Calibration and Performance of the AKARI Far-Infrared Surveyor (FIS) — Slow-Scan Observation Mode for Point-Sources

Mai Shirahata,[1] Shuji Matsuura,[1] Sunao Hasegawa,[1] Takafumi Ootsubo,[1] Sin'itirou Makiuti,[1]
Issei Yamamura,[1] Takao Nakagawa,[1] Mitsunobu Kawada,[2] Hidehiro Kaneda,[2]
Hiroshi Shibai,[3,2] Yasuo Doi,[4] Toyoaki Suzuki,[5] Thomas Müller,[6] and Martin Cohen[7]

[1]*Institute of Space and Astronautical Science (ISAS), Japan Aerospace Exploration Agency (JAXA),
3-1-1 Yoshinodai, Sagamihara, Kanagawa 229-8510*
sirahata@ir.isas.jaxa.jp
[2]*Graduate School of Science, Nagoya University, Furo-cho, Chikusa-ku, Nagoya 464-8602*
[3]*Graduate School of Science, Osaka University, 1-1 Machikaneyama-cho, Toyonaka-shi, Osaka 560-0043*
[4]*Department of General System Studies, Graduate School of Arts and Science, The University of Tokyo,
3-8-1 Komaba, Meguro-ku, Tokyo 153-8902*
[5]*National Astronomical Observatory of Japan, National Institutes of Natural Sciences, 2-21-1 Osawa, Mitaka, Tokyo 181-8588*
[6]*Max-Plank-Institut für extraterrestrische Physik, Giessenbachstrasse, 85748 Garching, Germany*
[7]*Radio Astronomy Laboratory, 601 Campbell Hall, University of California, Berkeley, CA 94720, USA*

Abstract

We present the characterization and calibration of the Slow-Scan observation mode of the Far-Infrared Surveyor (FIS) onboard the AKARI satellite. The FIS, one of the two focal-plane instruments on AKARI, has four photometric bands between 50–180 μm with two types of Ge:Ga array detectors. In addition to the All-Sky Survey, FIS has also taken detailed far-infrared images of selected targets by using the Slow-Scan mode. The sensitivity of the Slow-Scan mode is one to two orders of magnitude better than that of the All-Sky Survey, because the exposure time on a targeted source is much longer. The point spread functions (PSFs) were obtained by observing several bright point-like objects, such as asteroids, stars, and galaxies. The derived full widths at the half maximum (FWHMs) are $\sim 30''$ for the two shorter wavelength bands and $\sim 40''$ for the two longer wavelength bands, being consistent with those expected by optical simulation, although a certain amount of excess is seen in the tails of the PSFs. A flux calibration was performed by observations of well-established photometric calibration standards (asteroids and stars) over a wide range of fluxes. After establishing the method of aperture photometry, the photometric accuracy for point-sources is better than $\pm 15\%$ in all of the bands, expect for the longest wavelength.

Key words: instrumentation: detectors — methods: data analysis — space vehicles — techniques: photometric

1. Introduction

AKARI is the first Japanese satellite dedicated to infrared astronomy (Murakami et al. 2007). It was successfully launched on 2006 February 21 (UT) from the Uchinoura Space Center (USC) with the M-V rocket of Japan Aerospace Exploration Agency (JAXA). AKARI opened its aperture lid to begin astronomical observations on 2006 April 13. AKARI achieved continuous observations during 550 days by the time when the liquid-helium ran out on 2007 August 26. AKARI was thrown in a sun-synchronous polar orbit along the twilight zone at an altitude of ~ 700 km in order to carry out the All-Sky Survey in every half-year. The telescope has a size of 68.5 cm in diameter (Kaneda et al. 2007), and is cooled down at lower than 6 K in a liquid-helium cryostat (Nakagawa et al. 2007) for reducing thermal emission from the instruments.

The Far-Infrared Surveyor (FIS) is one of the two focal-plane instruments onboard AKARI (Kawada et al. 2007). It has four photometric bands between 50–180 μm, with two types of Ge:Ga array devices: the Short-Wavelength (SW) detector and the Long-Wavelength (LW) detector. The SW detector (Fujiwara et al. 2003), which is responsible for the

wavelength range in 50–110 μm, is a two-dimensional monolithic Ge:Ga photoconductor array. This array is directly connected to cryogenic readout electronics (CRE) by Indium-bumping technology. This detector was developed under collaboration among the National Institute of Information and Communications Technology (NICT), Institute of Space and Astronautical Science (ISAS) of Japan Aerospace Exploration Agency (JAXA), and Nagoya University. On the other hand, the LW detector (Doi et al. 2002) for 110–180 μm is a compact stressed Ge:Ga photoconductor array having a special cavity structure and a stressing mechanism. Ge:Ga chips for the LW detector were supplied by NICT, and the LW detector module was assembled by the University of Tokyo. As for the CREs of the SW and LW detectors, we developed a Capacitive Trans-Impedance Amplifier (CTIA) with silicon p-MOSFETs optimized for low-temperature operation (Nagata et al. 2004). FIS was designed primarily to perform the All-Sky Survey, which is the main purpose of the AKARI mission. Additionally, FIS has two other operation modes with pointing attitude control: the Slow-Scan mode to take detailed images of specific targets, and the spectroscopy mode to take spectra by using a Fourier transform spectrometer (Kawada et al. 2008;

N. Murakami et al. in preparation). The sensitivity in the Slow-Scan mode is 1–2 orders of magnitude better than that of the All-Sky Survey, because the exposure time on a target source is longer than that of the All-Sky Survey mode. In this paper, we describe the data-reduction procedures and the in-orbit performance of the Slow-Scan mode, the imaging performance, and a flux calibration.

The characterization and calibration of FIS were performed by observing two kinds of well-established photometric calibration standards. One of them was solar-system objects, such as asteroids and planets, and the others were stars. These calibration sources were studied well enough (asteroids: Müller & Lagerros 1998, 2002; stars: Cohen et al. 1999, 2003a, 2003b), and were used as a calibration standard in the previous infrared missions (e.g., ISO/ISOCAM: Blommaert et al. 2003; ISO/ISOPHOT: Schulz et al. 2002; COBE/DIRBE: Hauser et al. 1998, and Spitzer/MIPS: Gordon et al. 2007; Stansberry et al. 2007). Some of the galaxies observed by ISO and IRAS were also examined not only for cross calibration, but also for a calibration check for objects with much redder spectra than these of stars and asteroids.

In section 2, we explain the method of the FIS Slow-Scan observation. We describe observations of the calibration standards in section 3. Careful data-reduction procedures are required in order to obtain high-quality images and to establish accurate calibration. Accordingly, we describe the process of data reduction in section 4. The imaging performance is discussed in section 5. In section 6, we describe the calibration factors, and their flux dependency by considering the characteristics of the Ge:Ga detectors. We also checked the consistency of the calibration for various observations. Finally, we summarize our results in section 7. The calibration factors derived by the present work are the official values of the AKARI/FIS Slow-Scan calibration.

2. FIS Slow-Scan Observation

The FIS has four photometric bands whose center wavelengths are represented at 65, 90, 140, and 160 μm. These band shapes, shown in figure 1, are formed by the combination of optical filters and two detector devices. Each detector device covers one broad-band and one narrow-band: *WIDE-S* (90 μm) and *N60* (65 μm) for the SW detector and *WIDE-L* (140 μm) and *N160* (160 μm) for the LW detector. The array formats are 3×20, 2×20, 3×15, and 2×15 for the *WIDE-S*, *N60*, *WIDE-L*, and *N160* bands, respectively. The pixel scales are

26″.8 for the SW detector and 44″.2 for the LW detector, whose values are comparable to the diffraction limits of the telescope. The field-of-views (FOVs) of two detector devices overlap on the sky. The specifications for the FIS instrument are summarized in table 1.

As reported by many authors, Ge:Ga detectors show a slow transient response at low temperature under low background flux conditions, i.e., in the space environment (Kaneda et al. 2002; Hiromoto & Fujiwara 1999; Haegel et al. 1999; Fouks & Schubert 1995, and references therein). This slow transient response indicates the time-delay in the response for quick changes of the incoming flux. The time constant of the slow response is typically 10–100 s, and depends on both the background and the signal-photon fluxes. Therefore, in the case of AKARI, which conducts scan observations, the slow response causes a decrease of the sensitivity for compact sources. In order to reduce the effects of the slow response of the LW detector, an offset light source is placed in front of the LW detector unit to irradiate each detector pixel with a constant intensity. The intensity of this offset light source was set to be $\sim 100\,\mathrm{MJy\,sr^{-1}}$ to obtain the highest signal-to-noise ratio taking the increase of the photon noise into account.

FIS Slow-Scan observations are carried out using the AKARI astronomical observation templates (AOTs) FIS01 and FIS02. FIS01 is designed for compact source photometry with
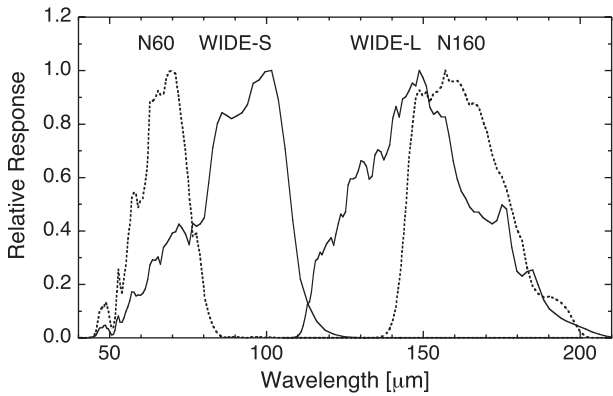

Fig. 1. System spectral response of the FIS photometric bands. These profiles were derived from the spectral response of optical components and the detector spectral responsivity. These profiles provide the typical band shape, because detectors have a pixel-to-pixel variation of the spectral responsivity.

Table 1. Specification for the FIS instrument in the photometry mode.

Band name	*N60*	*WIDE-S*	*WIDE-L*	*N160*	
Center wavelength	65	90	140	160	[μm]
Wavelength range	50–80	60–110	110–180	140–180	[μm]
Array format	20×2	20×3	15×3	15×2	[pixels]
Pixel scale*	26″.8 × 26″.8		44″.2 × 44″.2		
Pixel pitch*	29″.5 × 29″.5		49″.1 × 49″.1		
Detector device	Monolithic Ge:Ga array		Stressed Ge:Ga array		

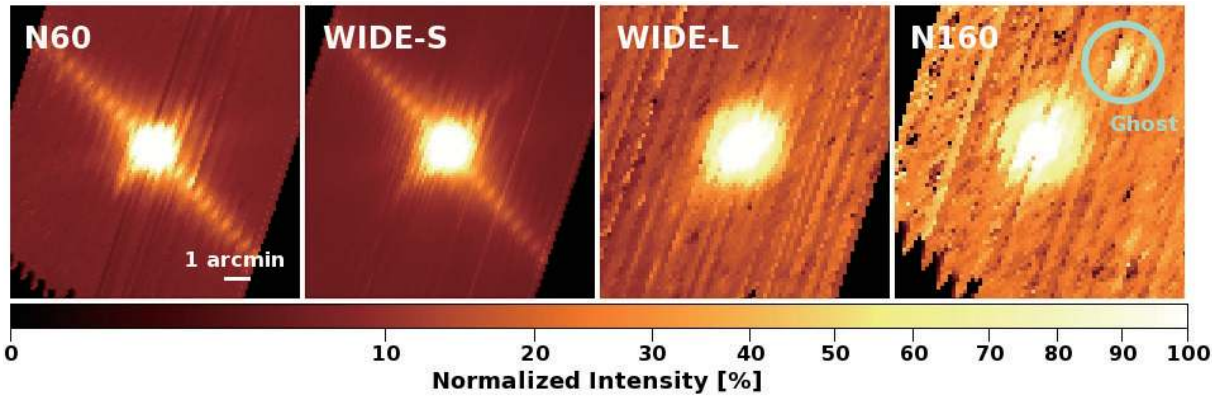* At the center of the field of views.

Fig. 2. Examples of the final co-added image obtained by the FIS Slow-Scan observation mode (AOT FIS01). The panels show *N60*, *WIDE-S*, *WIDE-L*, and *N160* images from left to right. The image size is $10' \times 10'$. The color scale is square-root contours. In the images of the *N60* and *WIDE-S* bands, cross-talk signals are seen along both array axes. Ghost signals are seen in all bands, especially in the *N160* band.

two sets of round-trip scans, while FIS02 is suitable for wide-area mapping with a long single round-trip scan. Observers can select the scan speed ($8'' \, \mathrm{s}^{-1}$ or $15'' \, \mathrm{s}^{-1}$) and the reset interval (0.5 s, 1.0 s, or 2.0 s). In the case of FIS01, the cross-scan shift length between two round trips is also selectable from either a few pixels ($70''$) or half of the FOV ($240''$). More details about the AOTs are described in Kawada et al. (2007) and E. Verdugo et al. (2007).[1]

One set of the Slow-Scan observation takes about 30 minutes, including the calibration sequence. A dark-current measurement and a responsivity check with an internal calibrator are executed by closing the cold shutter during 7 minutes of the attitude maneuver operation between the All-Sky Survey position and the target position of the pointing observation. After the maneuver has been completed, the shutter is opened for monitoring the sky signal during the settling time for fine control of the satellite attitude, and then the Slow-Scan starts. At the turning point(s) of the round-trip scan(s), the shutter is briefly closed and the internal calibration lamps are turned on to monitor the time variation of the detector responsivity. The total observation time for the round-trip scan(s) is about 12 minutes. The same calibration sequence is repeated during the maneuver for returning to the All-Sky Survey mode after a pointing observation. Such a highly-redundant calibration data set enabled us to correct the response changes of the detectors, while referring to astronomical calibration data taken by separate observations with the same calibration sequence.

3. Targets

To evaluate the imaging performance and flux calibration, several kinds of astronomical point-like sources were observed: 18 Slow-Scan observations of 14 stars, 17 Slow-Scan observations of 11 asteroids, 2 Slow-Scan observations of a planet (Neptune), and 13 Slow-Scan observations of 11 galaxies. All observations were carried out by the FIS01 (two round-trip scans) mode with a $70''$ shift. The scan speed was $8'' \, \mathrm{s}^{-1}$ for

most cases to obtain a high signal-to-noise ratio. A few observations were performed with the $15'' \, \mathrm{s}^{-1}$ scan in order to check the influence caused by differences of the scan speed. The reset interval was chosen so as to avoid saturation for each target.

The calibration stars were selected from the standard star catalog for spectral types of A V and K III established by Cohen et al. (1999, 2003a, 2003b). These stars have been studied extensively, and are reliable as calibration standards with accuracies better than 6%. Unfortunately, the stars are too faint to be used as calibrators for the *WIDE-L* and *N160* bands.

Since asteroids are brighter than stars, they are widely used as far-infrared calibrators (Müller & Lagerros 2003). We used them for the *N60* and *WIDE-S* bands, and also for the *WIDE-L* and *N160* bands. Asteroids show flux variations on various levels and time scales due to changes of the illumination, observing geometries, and also their rotation. Therefore, we estimated the expected flux for each observation from a thermophysical model (TPM) (Müller & Lagerros 1998, 2002) by taking the geometries and surface properties into account. The flux uncertainties (see table 2) are based on a thorough analysis of the TPM input parameters and the number and quality of well-calibrated thermal observations for each asteroid. The apparent motions of the asteroids are typically less than $1' \, \mathrm{hr}^{-1}$, and are taken into account at image co-addition (see figure 2).

We also observed several point-like galaxies (luminous infrared galaxies) whose fluxes have been well studied by IRAS and ISO. We used bright samples for measuring the point spread functions (PSFs) and the encircled energy functions, especially for the *N160* band.

Table 2 summarizes the observation log and the expected fluxes with their uncertainties. In all four bands, the expected fluxes range from ~ 100 mJy to ~ 100 Jy, i.e., more than three orders of magnitudes. Note that the expected fluxes listed here are color-corrected values by assuming a flat spectrum (i.e., $\nu F_\nu = \mathrm{const.}$). All observations had been carried out in the performance verification (PV) phase and within the engineering time available for calibration, which is occasionally allocated according to the requirement.

[1] AKARI FIS Data Users Manual ver. 1.3 ⟨http://www.ir.isas.jaxa.jp/AKARI/ Observation/#IDUM⟩.

Table 2. Observation log and expected flux.*

Target name	Observation		Expected flux[†]				
	Date	AOT parameter[‡]	N60 [Jy]	WIDE-S [Jy]	WIDE-L [Jy]	N160 [Jy]	Accuracy [%]
HR 5826	2006/04/21 20:38:35	2.0;8;70	0.338	0.237	0.064	0.052	6
HR 5321	2006/04/22 06:31:28	2.0;8;70	0.276	0.193	0.053	0.043	6
HR 5321 (2)	2006/04/22 11:28:30	2.0;8;70	0.276	0.193	0.053	0.043	6
HR 5430	2006/04/28 04:27:17	2.0;8;70	0.543	0.380	0.104	0.084	6
HR 5430 (2)	2006/04/28 06:06:18	2.0;8;70	0.543	0.380	0.104	0.084	6
HR 1208	2006/04/29 15:57:40	1.0;8;70	2.864	2.006	0.545	0.441	6
HR 872	2006/04/30 00:11:43	2.0;8;70	0.214	0.150	0.041	0.033	6
HR 872 (2)	2006/04/30 01:50:45	2.0;8;70	0.214	0.150	0.041	0.033	6
HR 1208 (2)	2006/05/02 01:43:26	1.0;8;70	2.864	2.006	0.545	0.441	6
Alpha CMa	2006/10/07 18:28:06	2.0;8;70	3.290	**2.293**	0.616	0.497	1.47
Alpha Boo	2007/01/15 00:02:26	1.0;8;70	**18.689**	**13.089**	3.558	2.879	6
Alpha Tau	2007/02/28 14:18:57	1.0;8;70	**17.042**	**11.939**	3.249	2.630	6
HD 216386	2007/06/03 01:05:46	2.0;8;70	2.177	1.524	0.414	0.335	6
HD 98118	2007/06/10 01:17:14	2.0;8;70	0.330	0.232	0.063	0.051	6
HD 222643	2007/06/11 01:23:08	2.0;8;70	0.142	0.099	0.027	0.022	6
HD 224935	2007/06/20 00:48:29	2.0;8;70	1.869	1.309	0.355	0.288	6
HD 053501	2007/07/13 02:52:02	2.0;8;70	0.175	0.122	0.033	0.027	6
HD 92305	2007/08/23 12:12:43	2.0;8;70	0.906	0.636	0.173	0.140	6
241 Germania	2006/04/27 15:44:31	0.5;8;70	8.958	**6.932**	2.356	1.940	12.5
241 Germania (2)	2006/04/27 23:59:37	0.5;8;70	7.813	**6.064**	2.073	1.707	12.5
6 Hebe	2006/04/30 03:07:09	0.5;8;70	**25.258**	**19.382**	6.469	5.313	5
6 Hebe (2)	2006/05/01 00:34:26	0.5;8;70	**25.681**	**19.699**	6.570	5.396	5
511 Davida	2006/05/02 22:50:20	0.5;8;70	**18.394**	**14.387**	4.999	4.127	7.5
511 Davida (2)	2006/05/03 12:02:32	0.5;8;70	**18.185**	**14.214**	4.933	4.071	7.5
7 Iris	2006/08/01 18:19:43	0.5;8;70	56.355	42.927	14.103	11.554	20
2 Pallas	2006/09/27 06:20:31	0.5;8;70	**59.254**	**46.375**	16.142	13.329	10
1 Ceres	2006/11/08 14:58:11	0.5;8;70	**264.848**	**206.126**	**70.786**	**58.327**	5
93 Minerva	2006/11/20 00:42:13	1.0;8;70	7.551	**5.873**	2.017	1.662	7.5
65 Cybele	2006/12/28 00:16:17	1.0;8;70	**15.192**	**11.905**	4.155	3.431	5
4 Vesta	2007/02/23 22:33:11	0.5;8;70	**200.598**	**147.871**	**44.748**	36.486	7.5
4 Vesta (2)	2007/02/24 00:12:31	0.5;15;70	**202.519**	**149.228**	**45.113**	36.778	7.5
52 Europa	2007/04/14 23:08:31	0.5;8;70	**24.150**	**18.807**	6.467	5.328	5
52 Europa (2)	2007/04/15 22:19:51	0.5;15;70	**24.328**	**18.941**	6.511	5.364	5
Neptune	2007/05/13 01:22:57	0.5;8;70	**315.942**	**361.867**	**265.605**	**248.897**	5
Neptune (2)	2007/05/13 19:36:26	0.5;15;70	**316.215**	**362.171**	**265.833**	**249.113**	5
47 Aglaja	2007/06/26 01:48:04	2.0;8;70	7.008	5.423	1.844	1.518	7.5
511 Davida (3)	2007/07/20 03:36:26	0.5;8;70	**20.743**	**16.175**	5.576	4.592	7.5
IRAS 08201+2801	2006/04/22 01:17:21	0.5;8;70	—	—	—	—	—
IRAS 08201+2801 (2)	2006/04/22 02:56:21	0.5;8;70	—	—	—	—	—
IRAS 08591+5248	2006/04/22 04:42:28	0.5;8;70	—	—	—	—	—
IRAS 08572+3915	2006/04/26 01:03:51	0.5;8;70	—	○	—	—	—
IRAS 08474+1813	2006/04/30 03:59:18	0.5;8;70	—	—	—	—	—
IRAS 08474+1813 (2)	2006/04/30 05:38:20	0.5;8;70	—	—	—	—	—
Arp 220	2006/08/06 06:45:02	0.5;8;70	○	○	○	○	—
Mrk 231	2006/12/01 19:20:05	0.5;8;70	○	○	—	—	—
IRAS 20100−4156	2007/04/16 23:17:36	1.0;8;70	—	○	—	—	—
UGC 05101	2007/04/22 12:44:18	0.5;8;70	○	○	—	—	—
IRAS 00188−0856	2007/06/23 01:45:19	2.0;8;70	—	○	—	—	—
IRAS 15250+3609	2007/07/28 03:16:26	2.0;8;70	—	○	—	—	—
IRAS 03158+4227	2007/08/23 11:35:18	2.0;8;70	—	○	—	—	—

* The data designated with the bold-faced or ○ symbol is data used for the measurements of PSFs and the encircled energy function.
[†] Model calculation: Stars: Cohen et al. (1999, 2003a, 2003b); Asteroids: Müller and Lagerros (1998, 2002); Neptune: Moreno (1998).
[‡] FIS01 AOT parameter: Reset interval [s]; scan speed [″ s^{-1}]; shift length [″].

4. Data Reduction

The raw data were processed using the official FIS slow-scan data-analysis toolkit (SS-tool) to produce time-series calibrated data and a final co-added map. More details about the standard reduction steps are described in Matsuura et al. (2007).

First of all, the raw data were processed by the software tools to do ADU-to-volt conversion, flagging of bad data (dead pixels, saturated pixels, reset anomalies, and other discontinuities) and the correction of non-linear integration ramps.

The next process is a slope calculation of each ramp, with removing cosmic-ray events identified in the ramp. This process maximizes the signal-to-noise ratio and avoids any periodic structure arising from incompleteness of the non-linear ramp correction. The reduced data provide 1–10 samples per pixel for a source crossing time, which depend on both the

scan speed and the reset interval. By co-adding the data of all array pixels, the Nyquist sampling condition is satisfied in the real-space domain. Glitches and subsequent tails induced by cosmic-ray hits affect the data severely (Suzuki et al. 2008). The integration ramps affected by the glitches were eliminated in the slope calculation process. The tails were not flagged-out at this stage, but the affected data were removed by sigma clipping in the co-addition process.

The third step of the SS-tool processing is to produce calibrated data for each array pixel after dark current subtraction and flat-fielding. The pixel-to-pixel variations of the detector responsivity are approximately 15% and 50% of the average for the SW detector and the LW detector, respectively. Therefore, a correction of the responsivity variation is necessary to obtain accurate images. This process is based on FIS observations of known diffuse sources: zodiacal emissions and interstellar dust emissions, which are expected to be smooth within the field of view. In this process we can also compare the sky brightness measured by the FIS with DIRBE/COBE, which provide a well-calibrated far-infrared sky map (S. Matsuura et al. in preparation). Accordingly, a unit conversion from the instrumental unit to the surface brightness is simultaneously performed.

The zodiacal emission is expected to be almost perfectly flat; their anisotropies on arcminute scales are less than 1% (Abraham et al. 1997). In the cases of the *N60* and *WIDE-S* bands, the sky brightness of almost the entire sky, except for the Galactic Plane regions is dominated by the zodiacal emission, and the contributions of galactic cirrus (interstellar dust) emission are expected to be negligible. Hence, the blank sky observed near the target source can be used for flat-fielding, as long as there is no bright source in there. The response distribution of the detector array pixels is derived from the average of time-series data during a Slow-Scan, where the average is calculated after removing data that exceed the 3-σ noise level for each pixel. The flat is built based on sky monitoring data acquired during the attitude-settling time just before the Slow-Scan observation. The flat-fielding is done by dividing the data by the response distribution. With this 'self' flat-fielding method, any stripes in the image caused by the flat field errors are buried under the random noise.

In the cases of the *WIDE-L* and *N160* bands, the detector signals are dominated by offset light implemented to improve the slow transient response of the stressed Ge:Ga. Although galactic cirrus emissions at high latitudes could be a flat source with moderate smoothness ($\sim 10\%$) and relatively high brightness, their signals are less than 10% of that of the offset light. The intensity distributions of the offset light at the aperture of the detector arrays are estimated from laboratory measurements to be uniform to within 10%. Hence, the 'self' flat-fielding method with an average sky signal including offset light was applied to correct the responsivity variation in the detector arrays, as was done for the *N60* and *WIDE-S* bands.

The final step of the SS-tool processing is co-addition of the calibrated time-series data onto a sky grid. The sky position of each data point is derived from the telescope boresight according to the satellite attitude and from the array pixel map on the focal-plane. The grid pixel sizes were set to 2″.5. A sufficient number of data point per grid pixel (> 5 on average)

is secured by considering the finite size of the detector array pixel (Drizzle method: Williams et al. 1996). In the co-adding process, small glitches and other artifacts were sigma-clipped with the standard deviation calculated at each grid pixel. The threshold for the sigma-clipping was set to 5-times the standard deviation. The fraction of the rejected data points in this process was less than 1% of the original data.

Figure 2 shows an example of the final co-added images (asteroid Ceres) for all the FIS bands. The imaging performance and flux calibration based on the obtained maps are discussed in the following section.

5. Imaging Performance

5.1. Point Spread Functions (PSFs)

Before the launch of AKARI, we checked the PSFs in the laboratory using a pin-hole source located on the focal-plane of the FIS optics (Shirahata et al. 2003). The measured PSFs were almost consistent with those expected from an optical simulation, though the uncertainty that originated in the measurement system was somewhat large. The PSFs, throughout the optics including the AKARI telescope, were evaluated in orbit by observations of bright point-sources. These sources were chosen with the condition that S/N for single pointing observation is better than 300, which are designated in table 2 by the bold-faced type or the circle symbols: 19 sources brighter than 10 Jy for the *N60* band, 28 sources brighter than 2 Jy for the *WIDE-S* band, 6 sources brighter than 20 Jy for the *WIDE-L* band, and 4 sources brighter than 50 Jy for the *N160* band. Figure 3 shows the azimuthally-averaged radial profiles of the measured PSFs, and compares them with the optical simulation model (Jeong et al. 2003). The averaged profiles are well reproduced by the two-component Gaussian functions, whose parameters are summarized in table 3. The full widths at the half maximum (FWHM) of the main Gaussian component are $32'' \pm 1''$, $30'' \pm 1''$, $41'' \pm 1''$, and $38'' \pm 1''$ for the *N60*, *WIDE-S*, *WIDE-L*, and *N160* bands, respectively. At the tails of the PSFs, there are significant excess compared with the optical simulation, whose contributions are about 20% of the total power. We did not see any significant dependence in the PSFs on the infrared color of the targets.

5.2. Cross-Talk and Ghost Signals

One property affecting the imaging quality is cross-talk between array pixels. This effect is seen only with the SW detector, which has a monolithic structure. In the maps of the SW detector (*N60* and *WIDE-S*) shown in figure 2, cross-talk signals are clearly seen along the detector array axes. The amplitude of the cross-talk signal is roughly 5% or less of the peak signal. One possibility to explain this phenomenon is carrier diffusion or internal-reflection in the Ge:Ga substrate.

Another concern in terms of the imaging quality is the presence of ghost signals. A ghost image appears in all bands near the target image, and is especially prominent for the *N160* band as shown in figure 2. The center positions of broad-band and narrow-band arrays have an angular separation of $\sim 6'$ in the scanning direction, and a ghost signal of each array appears at a separate time corresponding to the angular separation. Therefore, the ghost signal appears in one array when strong
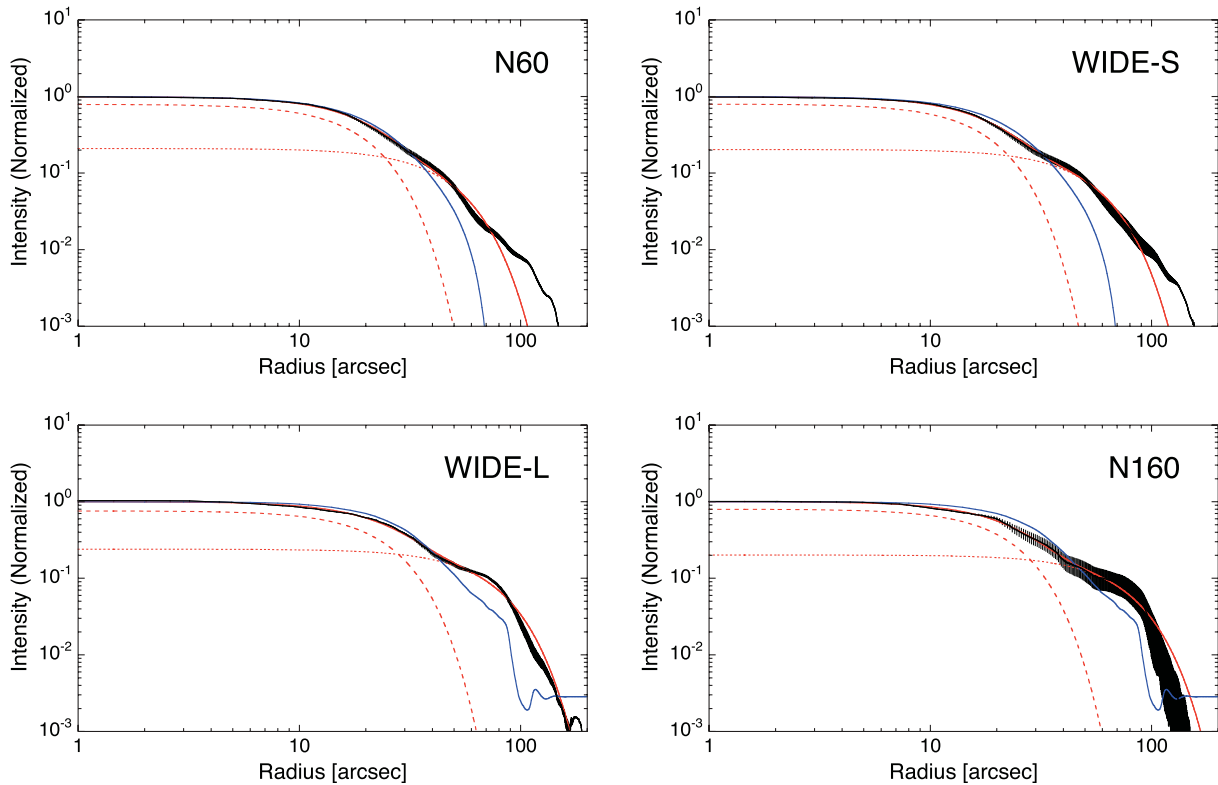
Fig. 3. Radial profiles of the observed PSFs and the optical simulation model. The observed profiles (black solid lines) are derived from the observation of bright point-sources. The error bars indicate the standard deviation. The results of the two-component Gaussian fitting are represented by red solid lines (total) and red dotted lines (each component). The expected profiles from the optical simulation model are shown by blue solid lines.

Table 3. Gaussian fitting parameters for the PSFs.*

Band name	N60	WIDE-S	WIDE-L	N160
Main component:				
- Intensity (A)	79.03%±0.33%	79.68%±0.23%	76.01%±0.38%	79.86%±0.30%
- FWHM (based on σ_1)	32.″05 ±0.″10	30.″17 ±0.″08	40.″85 ±0.″10	38.″23 ±0.″15
Sub component:				
- Intensity (1−A)	20.97%±0.35%	20.33%±0.24%	23.99%±0.39%	20.14%±0.30%
- FWHM (based on σ_2)	77.″51 ±0.″57	86.″01 ±0.″53	118.″98 ±1.″03	120.″62 ±0.″51

* Two-component Gaussian function: $I(x) = A \exp\left(-x^2/2\sigma_1^2\right) + (1-A) \exp\left(-x^2/2\sigma_2^2\right)$; A = Intensity of main component; $\sigma = \mathrm{FWHM}/2\sqrt{2\ln 2}$.

Table 4. Information of the ghost signal.*

Detector	SW (N60 ↔ WIDE-S)	LW (WIDE-L ↔ N160)
Relative position[†]		
- In-scan	5.′4	3.′6
- Cross-scan	0.′2	2.′0
- Distance	5.′4	4.′1
Intensity[‡]	∼1%	∼10%

* The ghost signal appears in one array when a strong light enters the other array of the same detector.
[†] The relative position of the ghost image from the target source.
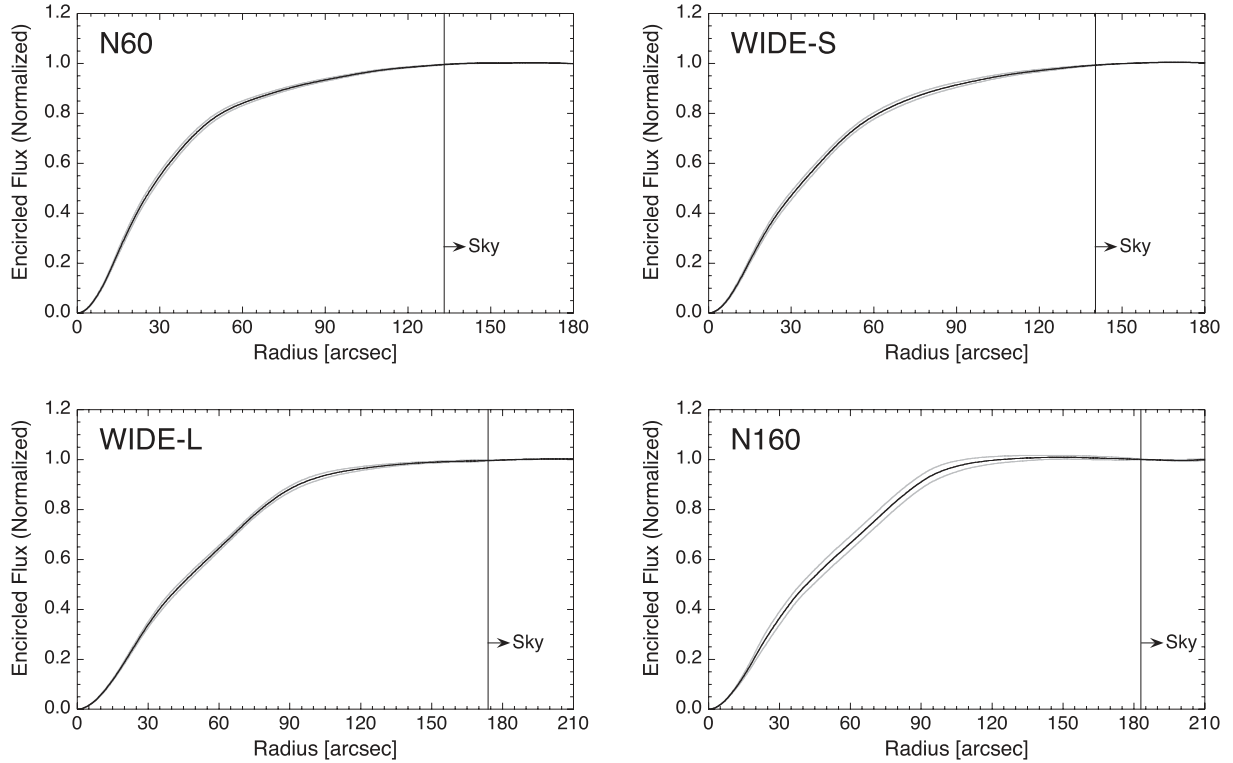[‡] The intensity of the ghost signal compared with the target signal observed in the other array.

Fig. 4. Encircled energy function. The gray region indicates the range of the standard deviation of sample. All profiles are normalized to 1.0 at the sky region.

light enters the other array of the same detector. The cause of the ghost is presumably electrical cross-talk in the multiplexer of the cryogenic readout electronics. The position and intensity of the ghost signal to the target signal, which are summarized in table 4, were stable throughout the mission. As long as the target is a point-source, the ghost should be removable.

6. Flux Calibration

6.1. Calibration Factor

As described in section 4, the final co-added maps produced by the SS-tool have units of surface brightness in MJy sr^{-1}, which was calibrated in the ealier stage in the data processing by diffuse sources, such as zodiacal emission and interstellar dust emission (S. Matsuura et al. in preparation). The application of aperture photometry for the co-added map gives the temporal flux of the target source. Hereafter, we derive the calibration factors for point-source photometry based on observations of the calibration standards.

For source extraction and aperture photometry, we used the photometry tools FIND, GCENTRD, and APER in the IDL Astronomy User's Library (Landsman 1993) at NASA/GSFC. These tools search for the center positions of point-sources with a Gaussian window function of the same width as the PSF, and measure the fluxes by integrating the pixel values within the aperture. The background sky levels were estimated to be the average of the surface brightness in the sky annulus, defined as 2.3–3.3 in radius for the *WIDE-S* and *N60* bands, and 3.0–4.0 for the *WIDE-L* and *N160* bands, respectively. The inner radius of the sky annulus is distant enough from the target

source, and the outer radius is distant enough from the edges of the maps.

Before performing aperture photometry for all of the calibration standards, we compounded the encircled energy functions from images of the bright sources that were used to measure the PSFs. First we computed the encircled energy for each source with various aperture radii, and then normalized the result at the background sky flux level. The obtained profiles of the encircled energy show good agreement with each other, within ∼3% for the shorter 3-bands and ∼6% for the *N160* band, as shown in figure 4. The aperture correction factors as the normalized encircled energy functions are summarized in table 5.

We performed aperture photometry on all images of the calibration standards by using an aperture radius of 40″ for the *WIDE-S* and *N60* bands, and 60″ for the *WIDE-L* and *N160* bands, respectively, and applied an aperture correction with the factors tabulated in table 5. These aperture radii are large enough to minimize uncertainties due to centroiding errors, and to ensure that any uncertainties in the aperture correction have a small effect on the derived fluxes. In addition, these aperture sizes enable us to improve the S/N of the photometry and thereby to extend the calibration to sources with somewhat fainter flux densities. We derived the uncertainty on each measurement from the scatter of the pixel values in the background annulus, which contributes both the uncertainty due to summing the object flux density as well as subtracting the background.

In order to derive the calibration factor for point-source photometry, we compared the observed fluxes obtained by

Table 5. Aperture correction factors.

Aperture*	N60	WIDE-S	WIDE-L	N160
5	0.030 ± 0.002	0.028 ± 0.002	0.015 ± 0.001	0.018 ± 0.001
10	0.112 ± 0.005	0.105 ± 0.006	0.056 ± 0.002	0.066 ± 0.003
15	0.225 ± 0.010	0.208 ± 0.010	0.116 ± 0.004	0.133 ± 0.009
20	0.340 ± 0.014	0.310 ± 0.014	0.187 ± 0.007	0.214 ± 0.018
25	0.440 ± 0.016	0.397 ± 0.016	0.264 ± 0.009	0.293 ± 0.025
30	0.524 ± 0.016	0.469 ± 0.017	0.337 ± 0.011	0.363 ± 0.026
35	0.596 ± 0.016	0.534 ± 0.016	0.402 ± 0.014	0.428 ± 0.026
40	0.659 ± 0.015	0.596 ± 0.016	0.458 ± 0.015	0.484 ± 0.026
45	0.715 ± 0.014	0.655 ± 0.015	0.507 ± 0.014	0.532 ± 0.027
50	0.762 ± 0.013	0.708 ± 0.014	0.554 ± 0.013	0.578 ± 0.028
55	0.799 ± 0.011	0.753 ± 0.014	0.599 ± 0.012	0.622 ± 0.028
60	0.826 ± 0.010	0.789 ± 0.013	0.644 ± 0.011	0.664 ± 0.028
65	0.847 ± 0.009	0.818 ± 0.013	0.689 ± 0.010	0.708 ± 0.028
70	0.865 ± 0.008	0.844 ± 0.013	0.734 ± 0.010	0.751 ± 0.028
75	0.882 ± 0.007	0.865 ± 0.012	0.778 ± 0.010	0.795 ± 0.028
80	0.897 ± 0.007	0.884 ± 0.012	0.817 ± 0.011	0.837 ± 0.028
85	0.911 ± 0.006	0.900 ± 0.011	0.852 ± 0.012	0.875 ± 0.028
90	0.923 ± 0.006	0.913 ± 0.010	0.881 ± 0.012	0.910 ± 0.027
95	0.934 ± 0.005	0.926 ± 0.009	0.904 ± 0.012	0.938 ± 0.026
100	0.944 ± 0.005	0.937 ± 0.008	0.922 ± 0.012	0.958 ± 0.024
105	0.954 ± 0.004	0.947 ± 0.007	0.936 ± 0.011	0.973 ± 0.022
110	0.963 ± 0.004	0.957 ± 0.006	0.948 ± 0.010	0.983 ± 0.019
115	0.971 ± 0.003	0.964 ± 0.005	0.956 ± 0.009	0.991 ± 0.017
120	0.977 ± 0.003	0.971 ± 0.005	0.963 ± 0.008	0.996 ± 0.015
125	0.982 ± 0.002	0.976 ± 0.004	0.969 ± 0.007	1.001 ± 0.013
130	0.987 ± 0.002	0.983 ± 0.003	0.975 ± 0.006	1.004 ± 0.012
135	0.991 ± 0.002	0.988 ± 0.002	0.979 ± 0.005	1.006 ± 0.010
140			0.983 ± 0.004	1.007 ± 0.009
145			0.986 ± 0.004	1.009 ± 0.008
150			0.989 ± 0.003	1.009 ± 0.007
155			0.991 ± 0.003	1.009 ± 0.007
160			0.992 ± 0.004	1.007 ± 0.007
165			0.994 ± 0.004	1.006 ± 0.007
170			0.995 ± 0.003	1.004 ± 0.006
175			0.996 ± 0.002	1.003 ± 0.005
180			0.998 ± 0.001	1.001 ± 0.003

* Aperture radius [″].

aperture photometry with their model prediction. Figure 5 shows the observed-to-expected flux ratios for the calibration standards as a function of the expected flux. Two asteroids (Germania and Iris) are excluded from the plot because of their poor model accuracies. The uncertainty on the flux ratios includes both photometric error and the expected model flux of the calibration standard. As shown in figure 5, even after an aperture correction, the observed fluxes are always lower than the expected ones. This means that the sensitivity to point-sources is lower than that to diffuse sources. In addition, the deviation seems to have a flux-dependency. A plausible cause of this disagreement is the slow transient response of the Ge:Ga detectors. Prior to the launch of AKARI, we had measured the slow response systematically under various photon flux conditions, and established an empirical model (Kaneda et al. 2002). According to this model, the slow response should depend on the total photo-current (background plus signal).

Figure 6 shows the observed-to-expected flux ratios, as a function of the total observed flux including the background. The observed background used here is the sum of the background sky brightness and the detector dark current. In order to convert the units of the background from MJy sr^{-1} to Jy, the beam solid angle derived from the PSF, which is summarized in table 6, is multiplied.

As described in section 2, the reset interval was changed, depending on the source flux. In figure 6, different symbols denote data with different reset intervals. Because no systematic differences were seen, we deal with these data equally.

In the SW bands, the background flux is so small that the total flux (TF) is dominated by the source flux. We can see a clear trend: the higher is the total flux, the smaller is the ratio. For bright sources, the ratio (R) is ~ 0.5, while for faint sources, it is ~ 0.8, although they show large scatter. The solid lines in figure 6 are the results of a power-law fitting to the data.
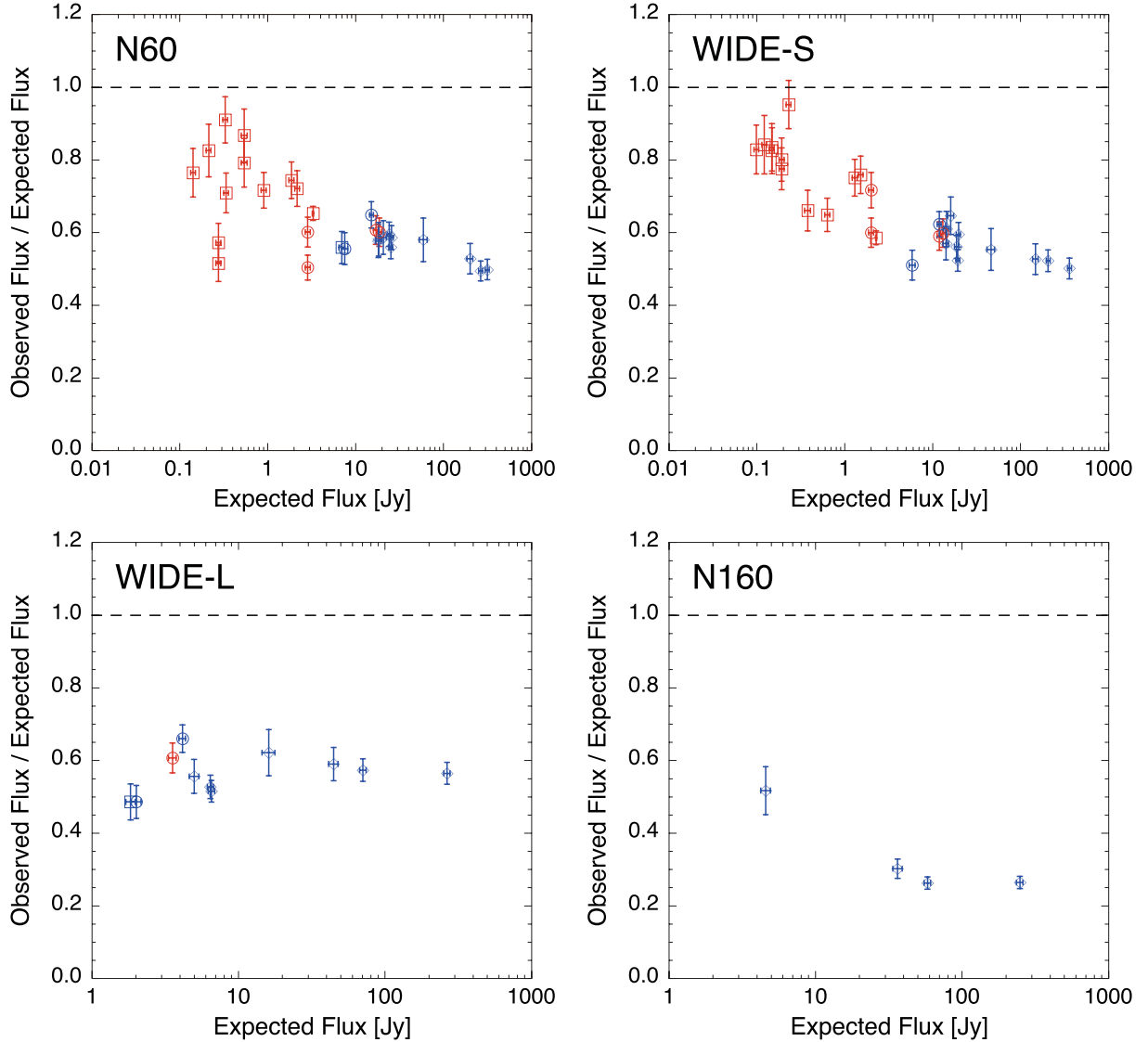
Fig. 5. The observed-to-expected flux ratio as a function of the expected flux. The error bars on the *y*-axis represent the combined uncertainty of measurement errors and model uncertainties. The red and blue symbols denote stars and asteroids, respectively. The squares, circles, and diamonds are the data with reset intervals of 2, 1, and 0.5 s, respectively. The dashed lines indicate a linear relation.

The fitting results give

$$R = (0.698 \pm 0.015) \times (TF)^{(-0.0659 \pm 0.0089)}$$
for the *N60* band,

$$R = (0.700 \pm 0.013) \times (TF)^{(-0.0757 \pm 0.0085)}$$
for the *WIDE-S* band. (1)

The deviations of the data from the power-law are reasonably small, 13.7% and 12.7% for the *N60* and *WIDE-S* bands, respectively. If we assume that the ratio is constant, the weighted means are 0.603 ± 0.007 and 0.607 ± 0.008 for the *N60* and *WIDE-S* bands, respectively, and the deviation increases to approximately 20% for both bands. Therefore, we conclude that there is a significant trend in the ratio with the total flux due to the slow transient response of the Ge:Ga detectors, and adopted the fitting results as the flux-dependent calibration factors.

In contrast to the case of the SW bands, the total fluxes in the LW bands are dominated by the offset light. Therefore, the total flux range is limited small, and the flux ratio does not show a clear flux dependence. Unfortunately for the *N160* band, a few data points does not give a firm conclusion but can suggest a trend as well as the *WIDE-L* band. No dependence of the flux ratio on the small flux range has been expected from an empirical model of stressed Ge:Ga photoconductor (Kaneda et al. 2002). The weighted means of the ratio in figure 6 are 0.560 ± 0.011 and 0.277 ± 0.011 for the *WIDE-L* and *N160* bands, respectively. The results show that the LW detectors have a much slower response than the SW detectors, despite that it uses offset light to improve the slow transient response. The deviations of the data from the weighted means are 9.97% and 50.5% for the *WIDE-L* and *N160* bands, respectively. The calibration accuracy of the *N160* band is much lower than that of the other bands, because of the small number of samples.
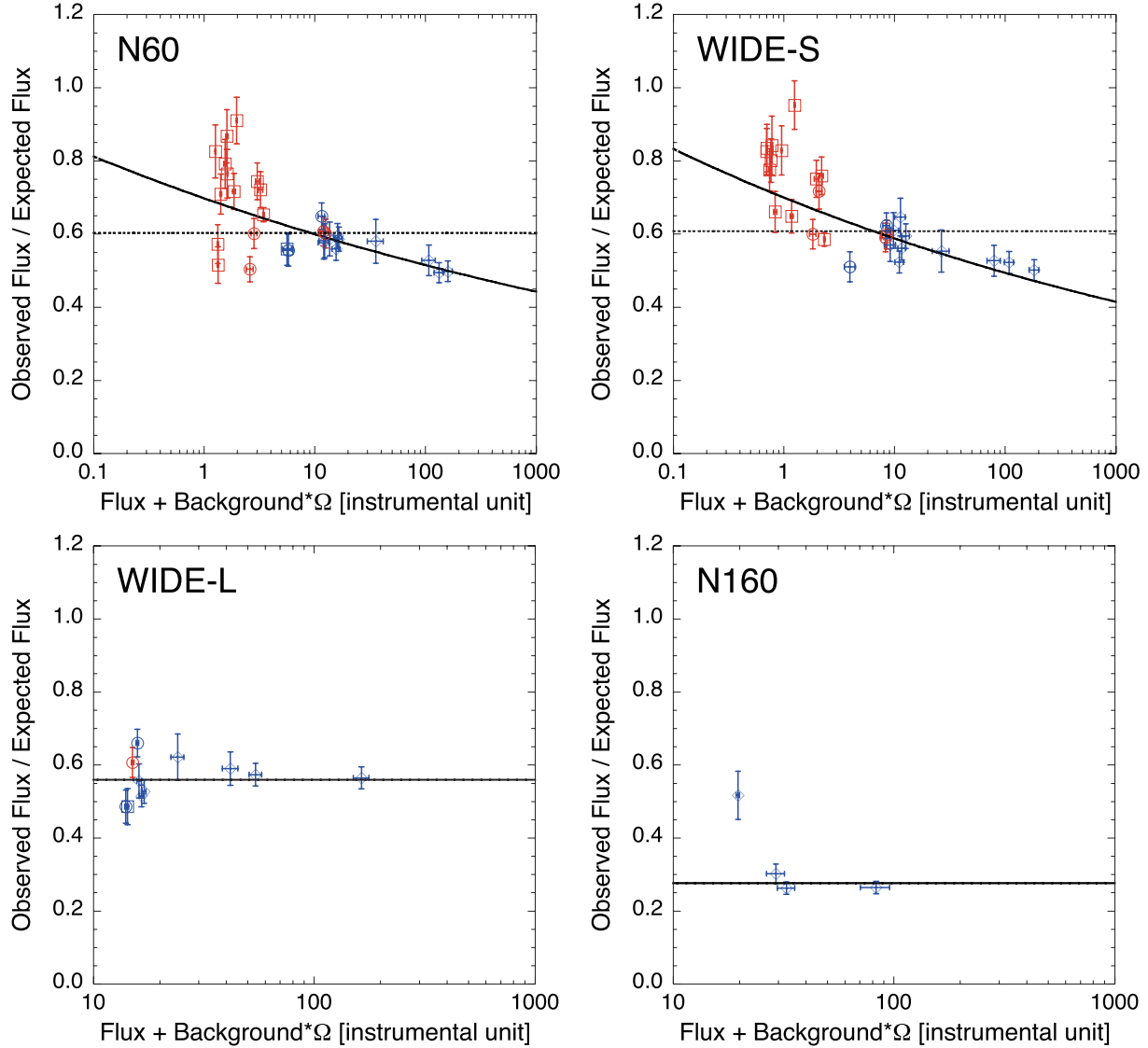
Fig. 6. The observed-to-expected flux ratio as a function of the total observed flux including the background flux and the dark current. The color and symbols are the same as those in figure 5. The solid lines for the SW bands are the results of a power-law fitting; $y = 0.698 \times x^{-0.0659}$ (*N60*), $y = 0.700 \times x^{-0.0757}$ (*WIDE-S*). The dashed lines for the SW bands and the solid lines for the LW bands are the weighted average; $y = 0.560$ (*WIDE-L*), $y = 0.277$ (*N160*).

Table 6. Beam solid angles.

Band name	Beam solid angle* [sr]
N60	$(4.06 \pm 0.10) \times 10^{-8}$
WIDE-S	$(4.81 \pm 0.13) \times 10^{-8}$
WIDE-L	$(9.92 \pm 0.19) \times 10^{-8}$
N160	$(10.21 \pm 0.42) \times 10^{-8}$

* The beam solid angles: $\pi r^2 /$ (Aperture correction factors at r); $r = 40''$ (for the *N60* and *WIDE-S* bands); $r = 60''$ (for the *WIDE-L* and *N160* bands).

6.2. Validity of the Calibration

In this subsection, we perform various checks on the calibrations, such as comparisons with previous missions, repeatability, the effects of the scan speed, and the observation mode.

The results of aperture photometry after applying the calibration factors derived above are listed in table 7.

6.2.1. Comparison with Previous Missions

In order to check the validity of the flux calibration, we observed the 11 galaxies listed in table 2, and compared their AKARI fluxes with those from IRAS and ISO.

All 11 galaxies were detected by IRAS at both 60 and $100\,\mu$m (IRAS Faint Source Catalog: Moshir et al. 1992). The predictions for the 65 and $90\,\mu$m fluxes based on the IRAS measurements were calculated as follows. First, we applied color corrections to the IRAS measurements (Beichman et al. 1988) by assuming a power-law spectrum. We then interpolated the IRAS 60 and $100\,\mu$m measurements to the center wavelength of the AKARI bands, 65 and $90\,\mu$m. Finally, we applied color corrections to the AKARI measurements by assuming the same power-law spectrum as that determined by the IRAS measurements. Figure 7 shows the IRAS-to-AKARI

Table 7. Results of observation.*

Target name	Observed flux [Jy]			
	N60	*WIDE-S*	*WIDE-L*	*N160*
HR 5826	**0.351± 0.013**	—	—	—
HR 5321	**0.208± 0.011**	**0.209± 0.007**	—	—
HR 5321 (2)	**0.230± 0.012**	**0.216± 0.008**	—	—
HR 5430	**0.696± 0.022**	—	—	—
HR 5430 (2)	**0.634± 0.020**	**0.354± 0.012**	—	—
HR 1208	**2.199± 0.064**	**1.798± 0.048**	—	—
HR 872	**0.257± 0.012**	**0.172± 0.007**	—	—
HR 872 (2)	—	**0.174± 0.007**	—	—
HR 1208 (2)	**2.641± 0.077**	**2.172± 0.058**	—	—
Alpha CMa	**3.337± 0.097**	**2.045± 0.056**	—	—
Alpha Boo	**19.009± 0.655**	**13.163± 0.403**	**3.855±0.101**	—
Alpha Tau	**17.452± 0.598**	**11.815± 0.360**	—	—
HD 216386	**2.430± 0.070**	**1.753± 0.047**	—	—
HD 98118	**0.450± 0.014**	**0.321± 0.009**	—	—
HD 222643	**0.161± 0.007**	**0.117± 0.005**	—	—
HD 224935	**2.143± 0.062**	**1.478± 0.039**	—	—
HD 053501	—	**0.144± 0.008**	—	—
HD 92305	**0.968± 0.028**	**0.596± 0.018**	—	—
241 Germania	10.249± 0.329	7.795± 0.226	2.806±0.109	—
241 Germania (2)	10.390± 0.334	7.855± 0.228	2.578±0.107	—
6 Hebe	**24.248± 0.865**	**17.382± 0.553**	—	—
6 Hebe (2)	**25.937± 0.934**	**20.272± 0.658**	**6.046± 0.156**	—
511 Davida	**18.076± 0.621**	**14.896± 0.465**	**4.966± 0.144**	—
511 Davida (2)	**17.690± 0.606**	**13.687± 0.423**	—	—
7 Iris	67.823± 2.803	57.474± 2.166	32.242±0.727	15.984±0.675
2 Pallas	**62.331± 2.544**	**46.987± 1.719**	**17.907±0.414**	—
1 Ceres	**258.977±12.991**	**219.497±10.082**	**72.467±1.619**	**55.259±2.286**
93 Minerva	**6.746± 0.208**	**4.749± 0.132**	**1.750±0.065**	—
65 Cybele	**16.579± 0.564**	**12.446± 0.380**	**4.897±0.122**	—
4 Vesta	**206.512±10.038**	**155.047± 6.779**	**47.163±1.064**	**39.749±1.652**
4 Vesta (2)	156.430± 7.310	117.833± 4.951	37.654±0.887	—
52 Europa	**24.736± 0.887**	**18.149± 0.582**	**6.093±0.168**	—
52 Europa (2)	22.525± 0.797	17.675± 0.565	5.879±0.260	—
Neptune	**314.872±16.229**	**384.606±19.106**	**267.687±5.937**	**238.428±9.814**
Neptune (2)	315.032±16.237	366.421±18.082	233.951±5.221	199.637±8.253
47 Aglaja	**6.289± 0.193**	—	**1.600±0.069**	—
511 Davida (3)	**20.701± 0.723**	**17.935± 0.572**	—	**8.568±0.420**
IRAS 08201+2801	1.054± 0.035	1.147± 0.032	—	—
IRAS 08201+2801 (2)	1.074± 0.033	1.128± 0.031	—	—
IRAS 08591+5248	0.630± 0.026	1.058± 0.030	—	—
IRAS 08572+3915	6.039± 0.184	5.494± 0.154	2.085±0.090	—
IRAS 08474+1813	1.241± 0.037	1.495± 0.039	0.572±0.062	—
IRAS 08474+1813 (2)	1.197± 0.036	1.461± 0.039	1.124±0.073	—
Arp 220	117.838± 5.280	137.905± 5.920	86.655±1.935	73.970±3.060
Mrk 231	30.019± 1.101	28.917± 0.983	20.411±0.461	17.709±0.738
IRAS 20100−4156	4.664± 0.139	4.896± 0.136	—	—
UGC 05101	10.570± 0.340	15.788± 0.494	15.529±0.358	13.973±0.584
IRAS 00188−0856	2.616± 0.076	2.599± 0.070	2.027±0.089	—
IRAS 15250+3609	5.958± 0.180	4.927± 0.136	—	—
IRAS 03158+4227	3.701± 0.109	3.961± 0.109	—	—

* The data designated with the bold-faced were used for the derivation of the calibration factors.
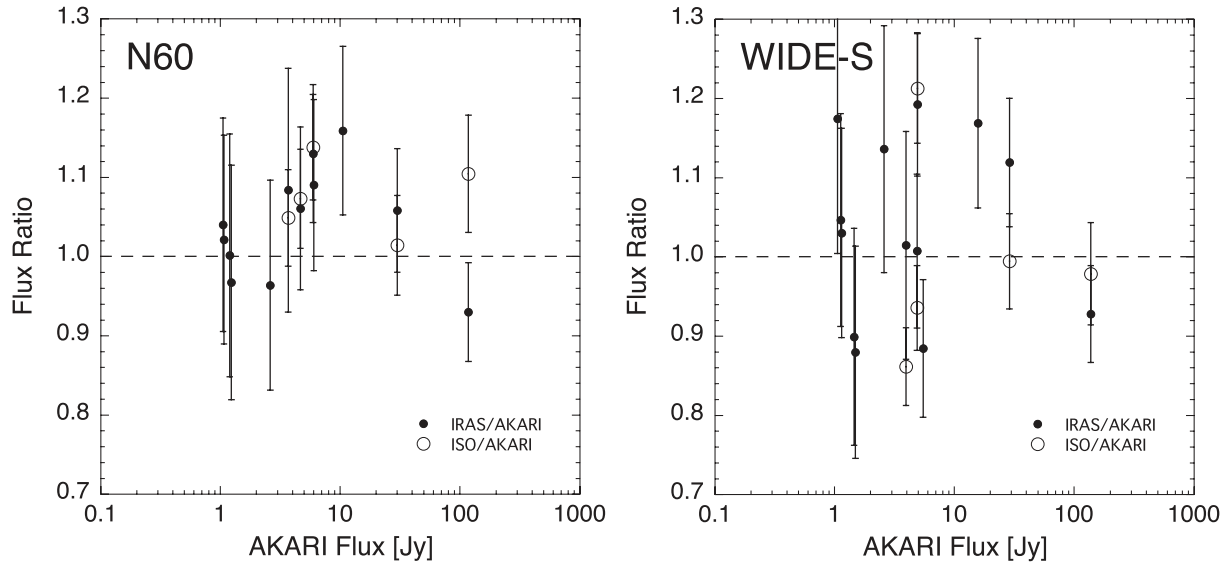
Fig. 7. Comparisons of AKARI flux with IRAS and ISO. The filled circles represent the flux ratio of IRAS-to-AKARI, while the opened circles represent the flux ratio of ISO/ISPHOTO-to-AKARI. The plots were not displayed for the *WIDE-L* and *N160* bands, because there were only two comparable data points.

flux ratios as a function of the AKARI flux. The average ratios of IRAS-to-AKARI measurements are 1.04 ± 0.03 and 1.03 ± 0.03 for the *N60* and *WIDE-S* bands, respectively. This result implies that the absolute calibration of both instruments is consistent with each other within the uncertainties.

Among our 11 samples, 5 famous galaxies (Arp 220, Mrk 231, IRAS 20100−4156, IRAS 15250+3609, IRAS 03158+4227) were observed by the ISO/ISOPHOT at 10 bands between 10 and 200 μm (Klaas et al. 2001). The wide wavelength coverage of ISO at longer than 100 μm enabled us to compare them not only in the SW bands, but also in the LW bands. We calculated the average ratios of ISO/ISOPHOT-to-AKARI by using the same method as that of IRAS-to-AKARI, but by assuming a gray-body spectrum given by the ISO/ISOPHOT measurement (Klaas et al. 2001), rather than a power-law spectrum. The results of the comparison are also shown in figure 7. The ratios of ISO/ISOPHOT-to-AKARI are 1.07 ± 0.03, 0.98 ± 0.03, 0.97 ± 0.13, and 0.89 ± 0.17 for the *N60*, *WIDE-S*, *WIDE-L*, and *N160* bands, respectively. Although the number of samples is not statistically sufficient, the obtained values are equal to unity within the uncertainties.

6.2.2. Repeatability

The photometric repeatability was checked by the data of stars and galaxies that were observed twice; asteroids are not suitable for repeatability checks because of the time-variations in their fluxes. In the case of the SW bands, 6 case studies (HR 5321, HR 5430, HR 872, HR 1208, IRAS 08201+2801, and IRAS 08474+1813) are available. Except for HR 1208, two measurements in each case agree to within 10% and 3% for the *N60* and *WIDE-S* bands, respectively. As for the *WIDE-L* and *N160* bands, since there is no comparable data, we could not check the photometric repeatability.

6.2.3. Scan Speed

In order to examine the dependence of the calibration factor on the scan speed, three calibrators (Vesta, Europa, and Neptune) were observed at scan speeds of both 8″ s^{-1} and

15″ s^{-1}. These data are listed in table 7. The observed fluxes for the 15″ s^{-1} data are ∼ 10% fainter than those for the 8″ s^{-1} data in all bands. This result implies a contribution of the slow transient response of the Ge:Ga detector. However, the number of samples is statistically insufficient to make any quantitative conclusion.

6.2.4. Observation Mode

The calibration factors derived here were determined from observations by using AOT FIS01 (two round-trip scans) with a 70″ shift length, but should also be applied directly to data taken with a 240″ shift length or with AOT FIS02 (single round-trip scan), because all of the modes conduct the same detector operation.

In order to evaluate the influence by the difference of the observation mode, we checked data for the far-infrared deep survey observed by the AKARI mission program team FBSEP (M. Shirahata et al. in preparation). They observed ∼ 2 deg^2 area with both FIS01 and FIS02 at scan speeds of 15″ s^{-1}, and detected 8, 126, 4, and 1 galaxies in the *N60*, *WIDE-S*, *WIDE-L*, and *N160* bands, respectively. The obtained fluxes are consistent with each other within 3%, 1%, 6%, and 10% for the *N60*, *WIDE-S*, *WIDE-L*, and *N160* bands, respectively, which are within the uncertainties. Therefore, we concluded that there are no significant differences originated in the observation mode.

6.3. Application to the Data Reduction

We note that our photometry is performed to a point-source with a fixed sky annulus: 2$'$.3–3$'$.3 in radius for the SW bands and 3$'$.0–4$'$.0 in radius for the LW bands. Therefore, the calibration factors presented here should only be applied to measurements carried out with the same parameters. Photometry using a different aperture size is possible via the application of an aperture correction factor (table 5), if the target is a point-source. If the target is an extended source, a proper treatment for the slow response is necessary.

Table 8. Summary of the calibration factors for point-source photometry.

Band name	Calibration factor*	Calibration accuracy [%]	Flux range† [Jy]
N60	$0.698 \times (TF)^{-0.0659}$	13.7	0.1–300
WIDE-S	$0.700 \times (TF)^{-0.0757}$	12.7	0.1–400
WIDE-L	0.560	9.97	0.5–300
N160	0.277	50.5	10 –250

* Total flux (TF) is a sum of the observed flux, background sky flux, and the detector dark current.
† Confirmed flux range. In the case of the fainter sources, the extrapolation should be possible, because the total fluxes are dominated by the detector dark current for the N60 and WIDE-S bands, and the offset light signal for the WIDE-L and N160 bands, respectively. The brighter end is almost comparable to the saturation limit.

Table 8 summarizes the calibration factors for point-source photometry in the FIS Slow-Scan observations. In order to measure the point-source fluxes, the signals integrated within the aperture must be divided by the calibration factor to correct the slow transient response. For point-sources brighter than 0.4, 0.1, 2.0, and 1.5 Jy in the N60, WIDE-S, WIDE-L, and N160 bands, respectively, uncertainties of the flux calibrations are larger than the measurement errors.

The FIS photometric flux is defined for a $\nu F_\nu = $ const. spectrum at the center wavelength of each band. This definition was first adopted by IRAS and used by several infrared astronomical satellites, such as COBE and ISO. Also, the Spitzer/IRAC and IRS instruments use the same convention, while the Spitzer/MIPS uses a 10000 K black-body as its reference spectrum. The flux obtained using these derived calibration factors is not the actual flux, but a 'quoted' flux. Therefore, in order to obtain the monochromatic flux at the band center wavelength, we should apply a color correction depending on the SED of the target source. A color correction factor, K, is defined as $K = \Delta\nu_{\text{SED}}/\Delta\nu_{\text{flat}} = F_{\text{obtained}}/F_{\text{real}}$, where $\Delta\nu$ is the effective band width. Color correction factors assuming a gray-body spectrum and a power-law spectrum are given in table 9.

7. Summary

We performed flux calibrations for the FIS Slow-Scan observations, based on measurements of stars and asteroids. We described in detail the data reduction and aperture photometric procedures that we used for the calibration sources. The expected fluxes of the calibration sources are lying in a wide flux range from 0.1 Jy to 400 Jy. There was a systematic flux dependence between the observed flux and the expected flux of the calibration sources, which was attributed to the slow transient response of the Ge:Ga detector. The calibration accuracies for the point-sources were estimated to be 14%, 13%, 10%, and 50% for the N60, WIDE-S, WIDE-L, and N160 bands, respectively. The calibration scheme described in this paper will be useful for future missions, such as Herschel and SPICA.

Table 9. Color correction factors.

Intrinsic spectrum	N60 (65 μm)	WIDE-S (90 μm)	WIDE-L (140 μm)	N160 (160 μm)
Black-body* ($\beta = 0$)				
- T = 10	4.434	1.840	1.549	1.097
- T = 30	1.050	0.892	0.957	0.986
- T = 50	0.976	0.979	0.937	0.986
- T = 70	0.978	1.066	0.935	0.988
- T = 100	0.992	1.154	0.935	0.989
- T = 300	1.029	1.320	0.936	0.992
- T = 1000	1.044	1.381	0.937	0.993
- T = 3000	1.048	1.398	0.937	0.993
- T = 10000	1.049	1.404	0.937	0.993
Gray-body* ($\beta = -1$)				
- T = 10	5.248	2.093	1.770	1.143
- T = 30	1.107	0.902	0.999	0.994
- T = 50	0.997	0.935	0.962	0.989
- T = 70	0.983	0.986	0.953	0.989
- T = 100	0.985	1.041	0.949	0.989
- T = 300	1.005	1.148	0.945	0.990
- T = 1000	1.013	1.187	0.944	0.990
- T = 3000	1.016	1.198	0.943	0.990
- T = 10000	1.016	1.202	0.943	0.990
Gray-body* ($\beta = -2$)				
- T = 10	6.281	2.396	2.048	1.198
- T = 30	1.178	0.930	1.060	1.008
- T = 50	1.030	0.918	1.003	0.998
- T = 70	1.001	0.944	0.987	0.995
- T = 100	0.992	0.976	0.978	0.994
- T = 300	0.995	1.041	0.968	0.993
- T = 1000	0.999	1.065	0.965	0.992
- T = 3000	1.000	1.072	0.964	0.992
- T = 10000	1.001	1.075	0.964	0.992
Power-law†				
- $\alpha = -3$	1.040	0.954	1.129	1.033
- $\alpha = -2$	1.013	0.962	1.054	1.013
- $\alpha = -1$	1.000	1.000	1.000	1.000
- $\alpha = 0$	1.001	1.076	0.964	0.992
- $\alpha = 1$	1.017	1.203	0.943	0.990
- $\alpha = 2$	1.049	1.407	0.937	0.993
- $\alpha = 3$	1.101	1.724	0.945	1.001

* Black-body and Gray-body spectrum : $F(\nu) \propto B_\nu(T) \cdot \nu^\beta$.
† Power-law spectrum : $F(\nu) \propto \nu^\alpha$.

References

Abraham, P., Leinert, C., & Lemke, D. 1997, A&A, 328, 702

Beichman, C. A., Neugebauer, G., Habing, H. J., Clegg, P. E., Chester, T. J. 1988, Infrared Astronomical Satellite (IRAS) catalog and atlases. Volume 1: Explanatory supplement (Washington, D.C.: NASA)

Blommaert, J. A. D. L., et al. 2003, The ISO Handbook, Vol.2, CAM– The ISO Camera, SP-1262, (Noordwijk: ESA)

Cohen, M., Megeath, S. T., Hammersley, P. L., Martín-Luis, F., & Stauffer, J. 2003a, AJ, 125, 2645

Cohen, M., Walker, R. G., Carter, B., Hammersley, P., Kidger, M., & Noguchi, K. 1999, AJ, 117, 1864

Cohen, M., Wheaton, Wm. A., & Megeath, S. T. 2003b, AJ, 126, 1090

Doi, Y., et al. 2002, Adv. Space Res., 30, 2099

Fouks, B. I., & Schubert, J. 1995, in Proc. SPIE, 2475, Infrared Detectors and Instrumentation for Astronomy, ed. A. M., Fowler, 2475, 487

Fujiwara, M., Hirao, T., Kawada, M., Shibai, H., Matsuura, S., Kaneda, H., Patrashin, M., & Nakagawa, T. 2003, Appl. Opt., 42, 2166

Gordon, K. D., et al. 2007, PASP, 119, 1019

Haegel, N. M, Simoes, J. C., White, A. M., & Beeman, J. W. 1999, Appl. Opt., 38, 1910

Hauser, M. G., Kelsall, T., Leisawitz, D., & Weiland, J. 1998, COBE Diffuse Infrared Background Experiment (DIRBE) Explanatory Supplement (Greenbelt: NASA)

Hiromoto, N., & Fujiwara, M. 1999, Infrared Phys. Technol., 40, 387

Jeong, W.-S., et al. 2003, PASJ, 55, 717

Kaneda, H., Kim, W., Onaka, T., Wada, T., Ita, Y., Sakon, I., & Takagi, T. 2007, PASJ, 59, S423

Kaneda, H., Okamura, Y., Nakagawa, T., & Shibai, H. 2002, Adv. Space Res., 30, 2105

Kawada, M., et al. 2007, PASJ, 59, S389

Kawada, M. et al. 2008, PASJ, 60, S389

Klaas, U., et al. 2001, A&A, 379, 823

Landsman, W. B. 1993, in ASP Conf. Ser., 52, Astronomical Data Analysis Software and Systems II, ed. R. J. Hanish, R. J. V. Brissenden, & J. Barnes (San Francisco: ASP), 246

Matsuura, S., et al. 2007, PASJ, 59, S503

Moreno, R. 1998, Ph.D. Thesis Université Paris VI

Moshir, M., Kopman, G., & Conrow, T. A. O. 1992, IRAS Faint Source Survey, Explanatory Supplement, ver. 2 (Pasadena: IPAC)

Müller, T. G., & Lagerros, J. S. V. 1998, A&A, 338, 340

Müller, T. G., & Lagerros, J. S. V. 2002, A&A, 381, 324

Müller, T. G., & Lagerros, J. S. V. 2003, in The calibration legacy of the ISO Mission, ed. L. Metcalfe, A. Salama, S. B. Peschke, & M. F. Kessler, SP-481, (Noordwijk: ESA) 157

Murakami, H., et al. 2007, PASJ, 59, S369

Nagata, H., Shibai, H., Hirao, T., Watabe, T., Noda, M., Hibi, Y., Kawada, M., & Nakagawa, T. 2004, IEEE Trans. Electron Devices, 51, 270

Nakagawa, T., et al. 2007, PASJ, 59, S377

Schulz, B., et al. 2002, A&A, 381, 1110

Shirahata, M., et al. 2003, in Proc. SPIE, 4859, Optical, Infrared, and Millimeter Space Telescopes, ed. J. C. Mather, 162

Stansberry, J. A., et al. 2007, PASP, 119, 1038

Suzuki, T., et al. 2008, PASP, 120, 895

Williams, R. E., et al. 1996, AJ, 112, 1335